

MOGO: Residual Quantized Hierarchical Causal Transformer for Real-Time and Infinite-Length 3D Human Motion Generation

Dongjie Fu*, Tengjiao Sun*, Pengcheng Fang*, Xiaohao Cai, Hansung Kim

Abstract—Recent advances in transformer-based text-to-motion generation have significantly improved motion quality. However, achieving both real-time performance and long-horizon scalability remains an open challenge. In this paper, we present MOGO (Motion Generation with One-pass), a novel autoregressive framework for efficient and scalable 3D human motion generation. MOGO consists of two key components. First, we introduce MoSA-VQ, a motion scale-adaptive residual vector quantization module that hierarchically discretizes motion sequences through learnable scaling parameters, enabling dynamic allocation of representation capacity and producing compact yet expressive multi-level representations. Second, we design the RQHC-Transformer, a residual quantized hierarchical causal transformer that decodes motion tokens in a single forward pass. Each transformer block aligns with one quantization level, allowing hierarchical abstraction and temporally coherent generation with strong semantic flow. Compared to diffusion- and LLM-based approaches, MOGO achieves lower inference latency while preserving high motion fidelity. Moreover, its hierarchical latent design enables seamless and controllable infinite-length motion generation, with stable transitions and the ability to adaptively incorporate updated control signals at arbitrary points in time. To further enhance generalization and interpretability, we introduce Textual Condition Alignment (TCA), which leverages large language models with Chain-of-Thought reasoning to bridge the gap between real-world prompts and training data. TCA not only improves zero-shot performance on unseen datasets but also enriches motion comprehension for in-distribution prompts through explicit intent decomposition. Extensive experiments on HumanML3D, KIT-ML, and the unseen CMP dataset demonstrate that MOGO outperforms prior methods in generation quality, inference efficiency, and temporal scalability.

I. INTRODUCTION

Text-to-motion generation is a rapidly evolving research area with growing importance in virtual environments, such as gaming, AR/VR, and humanoid robotics [1]. Recent advances have leveraged large language model (LLM)-based techniques to generate high-quality 3D human motion from text descriptions, typically using vector-quantized variational autoencoders (VQ-VAE) and autoregressive decoding strategies [2]–[5]. Meanwhile, diffusion-based approaches have also demonstrated strong generation performance, particularly in terms of motion fidelity and diversity [6].

Despite these achievements, both diffusion- and LLM-based frameworks face practical limitations [7]–[10]. Diffusion models often rely on iterative refinement processes, which

introduce significant inference latency and hinder their suitability for real-time or interactive applications [7]. On the other hand, LLM-based models, although autoregressive, typically involve large parameter sizes and long context dependencies, leading to high memory and computation costs that challenge deployment on lightweight scenarios [9]. A broader discussion of related research trends is provided in Section II.

To address the challenges of motion generation quality, inference efficiency, and generalization, we propose MOGO, a unified and efficient transformer-based framework for expressive text-to-motion synthesis. MOGO generates high-fidelity motion sequences from textual input in a single forward pass, combining structural compactness, temporal coherence, and extendable decoding. The framework is composed of four key components, each targeting a core aspect of the generation pipeline:

- We propose *MoSA-VQ*, a motion structure-aware quantization framework with two key innovations: (i) a learnable modulation mechanism that adaptively scales residual magnitudes across quantization levels, and (ii) a novel cross-level decorrelation loss that enforces statistical orthogonality between quantized vectors and subsequent residuals. Together, these components enable more compact and hierarchically disentangled representations, leading to better reconstruction under constrained codebook capacity.
- *RQHC-Transformer (Residual Quantized Hierarchical Causal Transformer)* functions as the motion decoder. It autoregressively generates multi-layer motion tokens in a single forward pass, with each transformer block dedicated to decoding one level of the quantized hierarchy. This design ensures temporally coherent synthesis while preserving decoding efficiency and compatibility with interactive applications.
- *Infinite-Length Generation* is enabled by the autoregressive nature of MOGO’s architecture. Unlike diffusion-based methods that require fixed-length sampling, MOGO supports seamless motion extension with consistent structure and fidelity, making it suitable for real-time or open-ended generation scenarios.
- *Textual Condition Alignment (TCA)* leverages large language models with Chain-of-Thought reasoning to bridge the gap between real-world user prompts and the model’s training distribution. Beyond simple style normalization, TCA explicitly decomposes complex motion instructions

* Equal Contribution.

† Corresponding author.

into structured semantic cues, enabling more accurate motion interpretation. This enhances MOGO’s generalization capability across both in-distribution and zero-/few-shot scenarios, while improving control fidelity and robustness to diverse user inputs.

II. RELATED WORK

Human Motion Generation. Recent advances in human motion generation have enabled conditioning on modalities like text, audio, music, and images [1]. Early deterministic models [11], [12] often produced over-smoothed, unrealistic motions. To address this, stochastic approaches, such as GANs [13], [14] and VAE-based models [15], [16], improved motion diversity. Text-to-motion generation gained prominence with works like [17], which used temporal VAEs to model text-motion distributions. Recently, diffusion-based methods [6], [8], [18]–[21] and transformer-based approaches [2], [3], [22] have led the field.

LLM-Based Motion Generation Models. LLM-based architectures have become a cornerstone of text-to-motion generation, leveraging their ability to model sequential data and adapt to varied tasks [2]–[5], [22]. Models like MoMask [2] and MMM [4] use masked token modeling to produce high-quality motions but struggle with extendable output and generalization in low-data or out-of-distribution settings due to their bidirectional design. Conversely, autoregressive models like T2M-GPT [3] and AttT2M [5] enable sequential generation, making them suitable for real-time applications and scalable with larger datasets, though they often sacrifice some motion quality. Efforts like MotionGPT [22] integrate multimodal language modeling but face challenges in achieving high-fidelity motion outputs. Our MOGO framework addresses these issues by combining efficient encoding through the MoSA-VQ with a single-pass autoregressive transformer, ensuring both high-quality motion and interactive capabilities.

Hierarchical Transformers. Hierarchical transformer architectures excel in domains like NLP [23], [24], image generation [25], and vision tasks [26], [27]. By processing data at multiple abstraction levels, these models enhance representation capacity and scalability. For instance, Swin Transformers [26] support scalable high-resolution vision, while CogView2 [25] enables high-fidelity image synthesis. In motion generation, hierarchical transformers are underexplored, especially for autoregressive frameworks with residual quantization. Our RQHC-Transformer in MOGO leverages hierarchical modeling to efficiently process multi-layer motion tokens, improving quality and generalization.

Motion Tokenization. Discretizing continuous motion data into tokens via vector quantization is central to transformer-based motion generation. TM2T [28] introduced VQ-VAE to map motions to discrete sequences. T2M-GPT [3] enhanced token quality with exponential moving average and codebook reset techniques. AttT2M [5] improved quantization through body-part-aware encoding. MoMask [2] advanced this with residual vector quantization (RVQ), producing multi-level tokens for better reconstruction quality. Compared to prior work, our approach introduces learnable feature scaling

into the residual vector quantization process, allowing each quantization level to adaptively adjust the magnitude of its residuals. This scaled RVQ mechanism stabilizes the residual distribution across quantization stages, mitigates the risk of later stages collapsing to noise, and ensures more effective codebook utilization. As a result, the model benefits from improved reconstruction fidelity, better token expressiveness, and enhanced training stability.

III. METHODS

A. Overview of the MOGO Framework

Our proposed framework, MOGO, as shown in Figure 1, consists of four key components designed for efficient and expressive text-to-motion generation. First, MoSA-VQ discretizes motion sequences into multi-level latent tokens using hierarchical residual quantization with adaptive scaling. Second, RQHC-Transformer autoregressively decodes the quantized representations with a stack of level-aligned transformer blocks. Third, MOGO supports infinite-length generation via seamless autoregressive extension. Lastly, we introduce TCA to enhance generalization to real-world prompts. We elaborate on each component in the following subsections.

B. MoSA-VQ: Motion Scale-Adaptive Residual VQ-VAE

To transform continuous human motion into discrete representations suitable for autoregressive generation, we build upon residual vector quantized variational autoencoders (RVQ-VAEs) and propose MoSA-VQ. While standard RVQ-based approaches [2], [5] hierarchically encode motion features through fixed-stage quantization, they often rely on manually tuned feature ranges and static scaling behavior, which limit their adaptability and quantization efficiency—especially in the presence of diverse and complex motions.

a) Adaptive Hierarchical Quantization.: To address these limitations, we introduce a learnable feature scaling mechanism into each quantization level. Specifically, each level is equipped with its own learnable scale and bias parameters, which dynamically adjust the amplitude and offset of the input residual features before quantization. This adaptive design allows each level to allocate representational capacity where needed, resulting in more effective codebook usage and higher reconstruction accuracy without the need for handcrafted calibration.

At each hierarchical quantization level $l \in \{0, 1, \dots, L\}$, the residual vector is first transformed using a learnable affine mapping. We denote this process as:

$$\mathbf{q}^l = \mathcal{Q}(\mathbf{W}^l \mathbf{r}^l + \mathbf{b}^l), \quad \phi^l = (\mathbf{W}^l)^{-1}(\mathbf{q}^l - \mathbf{b}^l), \quad (1)$$

where $\mathbf{W}^l \in \mathbb{R}^{d \times d}$ is a diagonal scaling matrix, $\mathbf{b}^l \in \mathbb{R}^d$ is a learnable bias vector, $\mathcal{Q}(\cdot)$ denotes nearest-neighbor quantization via a codebook, and ϕ^l represents the decoded contribution at level l .

This hierarchical quantization scheme enables progressive residual refinement. Unlike conventional residual vector quantization (RVQ) frameworks that apply uniform scaling across all levels, our design introduces level-specific adaptive modulation through learnable parameters \mathbf{W}^l and \mathbf{b}^l . This flexibility

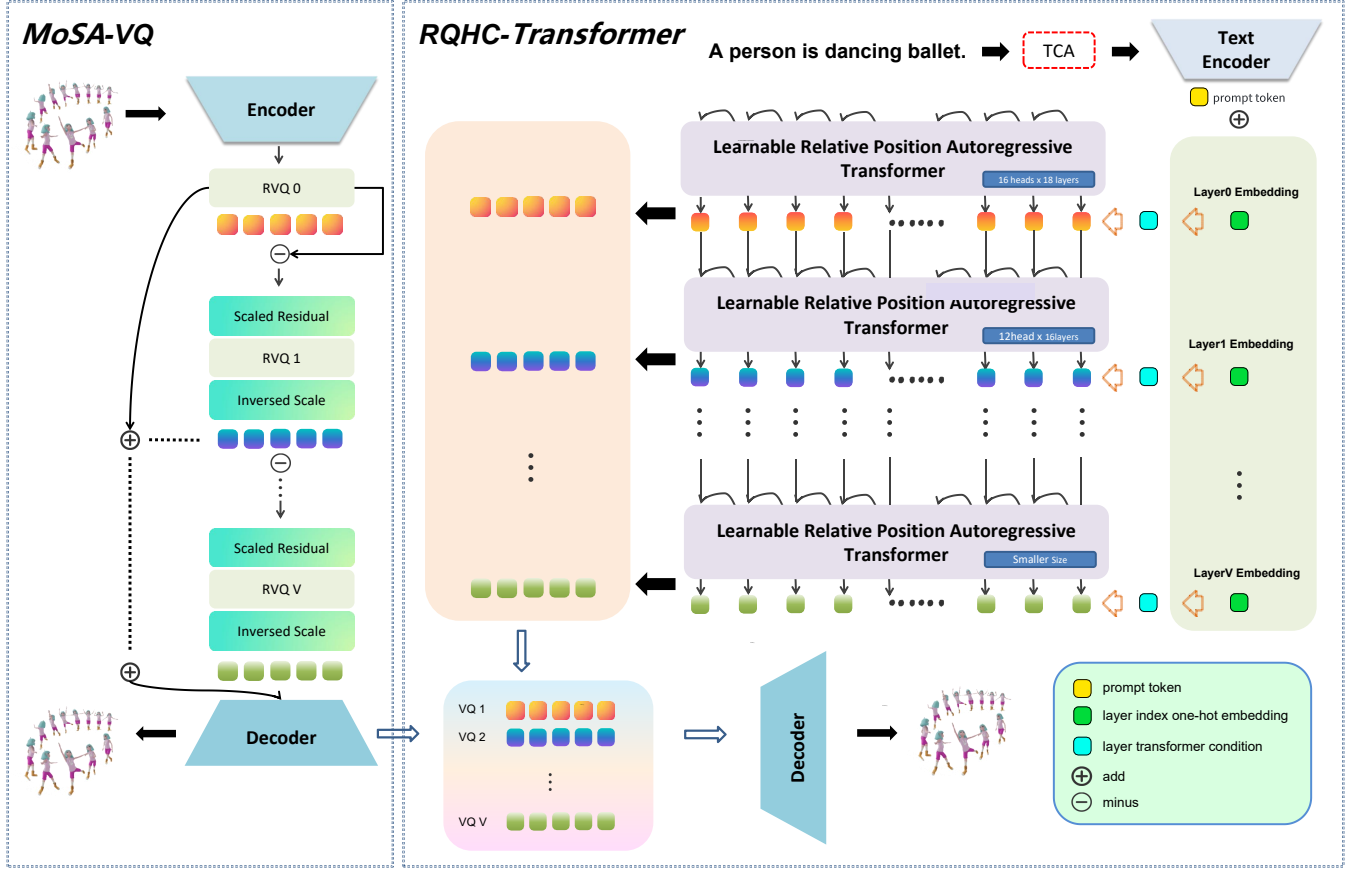


Fig. 1: Overview of the proposed MOGO framework. *Left*: We first encode the motion sequence using a hierarchical MoSA-VQ module with learnable feature scaling, indexing a multi-level codebook. *Right*: Then, tokens are autoregressively generated by a RQHC-Transformer with relative positional attention. Finally, the predicted token sequence is quantized and decoded into a full 3D human motion sequence.

allows coarse levels to capture global structure, while deeper layers focus on subtle motion or spatial details. The inverse affine transformation ensures consistent feature recovery, and stride-1 convolutions in both encoder and decoder maintain temporal continuity without aliasing artifacts. We have

$$\mathbf{r}^{l+1} = \mathbf{r}^l - \phi^l, \quad \hat{\mathbf{z}} = \sum_{l=0}^L \phi^l. \quad (2)$$

b) Training Objective.: Our full training objective combines four terms: motion reconstruction, codebook commitment, lightweight modulation regularization, and a novel cross-level decorrelation loss.

We adopt an ℓ_1 reconstruction loss to ensure accurate motion recovery, and a standard commitment loss to encourage the encoder residuals \mathbf{r}^l to remain close to their quantized counterparts ϕ^l . A mild regularization is also applied to the per-layer scaling and bias parameters $(\mathbf{W}^l, \mathbf{b}^l)$, following prior work on stable quantization with learnable modulation.

Additionally, we introduce a cross-level decorrelation loss, which explicitly penalizes statistical redundancy between the

quantized vector ϕ^l and the subsequent residual \mathbf{r}^{l+1} :

$$\mathcal{L}_{\text{decor}} = \sum_{l=0}^{L-1} \|\text{Cov}(\phi^l, \mathbf{r}^{l+1})\|_F^2.$$

This loss is motivated by the principle that, in an ideal residual quantization hierarchy, each level should encode novel information orthogonal to what has already been captured. A nonzero covariance between ϕ^l and \mathbf{r}^{l+1} indicates overlapping representation subspaces, leading to inefficient coding and excessive reliance on deeper quantizers. By minimizing their batch-wise covariance, we enforce an approximate statistical orthogonality between levels, which encourages disentangled information flow and hierarchical efficiency.

From an information-theoretic perspective, this decorrelation loss can be viewed as promoting minimal mutual information between consecutive encoding layers, thus maximizing the effective bit utilization of each quantized token. Empirically, we find this regularization yields more compact latent codes and improves reconstruction quality under constrained

codebook budgets. The final loss function is:

$$\begin{aligned} \mathcal{L}_{\text{vq}} = & \gamma \sum_{l=0}^L \left(\underbrace{\|\mathbf{W}^l - \mathbf{I}\|_F^2 + \|\mathbf{b}^l\|_2^2}_{\text{modulation reg.}} \right) + \beta \sum_{l=0}^L \underbrace{\|\mathbf{r}^l - \text{sg}[\phi^l]\|_2^2}_{\text{commitment}} \\ & + \lambda \sum_{l=0}^{L-1} \left(\underbrace{\|\text{Cov}(\phi^l, \mathbf{r}^{l+1})\|_F^2}_{\text{cross-level decorrelation}} \right) + \underbrace{\|\mathbf{m} - \hat{\mathbf{m}}\|_1}_{\text{reconstruction}}. \end{aligned} \quad (3)$$

Here, β , λ and γ are weight factors.

C. RQHC-Transformer: Residual Quantized Hierarchical Causal Transformer

To fully leverage the high-quality hierarchical representations produced by MoSA-VQ, we propose the Residual Quantized Hierarchical Causal Transformer (RQHC-Transformer), an autoregressive decoder structurally aligned with the residual quantization process. In contrast to single-resolution or per-layer decoding approaches, RQHC jointly models all quantization levels in a residual-aware and level-aware manner. Moreover, we adopt a causal Transformer design, which—compared to bidirectional transformers, LLM-style decoders, or iterative diffusion models—offers efficient one-pass inference, supports streamable generation, and naturally enables long-horizon synthesis. The coarse-to-fine decoding progression preserves structural semantics, mitigates token interference, and promotes stable, coherent motion generation with improved interpretability.

This hierarchical causal architecture progressively refines coarse motion structures, preserving semantic consistency across abstraction levels and reducing token-level interference. Crucially, its design is structurally aligned with the residual quantization process of MoSA-VQ, enabling stable information flow across layers. Together, this synergy allows MOGO to extend motion from any given frame with temporal continuity and semantic fidelity, laying the foundation for real-time, controllable infinite-length generation.

a) Hierarchical Causal Generation.: To generate the token sequence at quantization level l , we construct an input sequence \mathbf{s}^l that conditions on both the textual prompt and the residual context from lower levels:

$$\mathbf{s}^l = [\mathbf{p} + \mathbf{q}_{\text{emb}}, \mathbf{t}_l^{1:n}], \quad (4)$$

where \mathbf{p} is the CLIP-based text prompt embedding, and \mathbf{q}_{emb} is the embedding representing the current quantization level. The sequence $\mathbf{t}_l^{1:n}$ is computed by aggregating token embeddings across all previous levels at each position:

$$\mathbf{t}_l^{1:n} = [\text{Embed}(t_1^1), \text{Embed}(t_2^1), \dots, \text{Embed}(t_n^1)]. \quad (5)$$

Here, n denotes the number of motion tokens (i.e., temporal steps) in the sequence. Each t_i^l is the i -th quantized token at layer l , and $\text{Embed}(\cdot)$ maps each token to its corresponding embedding vector.

Relative Positional Encodings. To effectively handle long motion sequences, we incorporate a relative positional encoding scheme into our causal attention layers. Compared to absolute positional encodings, this approach better preserves

attention consistency for varying sequence lengths and enhances the model’s ability to capture long-range dependencies.

Given an input token sequence, the attention score between token i and token j is computed as:

$$\mathbf{A}_{i,j}^{\text{rel}} = \mathbf{q}_i^\top \mathbf{k}_j + \mathbf{q}_i^\top \phi_{i-j} + u^\top \mathbf{k}_j + v^\top \phi_{i-j}, \quad (6)$$

where \mathbf{q}_i and \mathbf{k}_j are the query and key embeddings at position i and j , and ϕ_{i-j} is a learned relative position embedding, and u and v are learnable global bias vectors. The final output of the self-attention is:

$$\mathbf{a}_i^n = \text{Softmax}(\mathbf{A}_i^n) \mathbf{V}_i^n, \quad (7)$$

where \mathbf{A}_i^n is the attention score matrix incorporating relative positional encoding at layer n of the l -th quantization level. \mathbf{V}_i^n denotes the value matrix at the same layer.

b) Training Objective.: To learn temporally coherent and hierarchically consistent token generation, we adopt a multi-layer autoregressive training objective defined over all quantization levels. The loss function is written as:

$$\mathcal{L}_{\text{ce}} = -\mathbb{E}_{(\mathbf{t}, c) \sim \mathcal{D}} \left[\sum_{l=1}^L \log p_\theta(\mathbf{t}^l \mid \mathbf{t}_{<}^l, c) \right], \quad (8)$$

where \mathcal{L}_{ce} denotes the total cross-entropy loss computed over all quantization levels. The training data \mathcal{D} consists of pairs (\mathbf{t}, c) , where $\mathbf{t} = \{\mathbf{t}^1, \dots, \mathbf{t}^L\}$ is the set of discrete motion token sequences across L quantization levels, and c is the global conditioning signal derived from the input text and the residual context from coarser levels. Each sequence $\mathbf{t}^l = (t_1^l, t_2^l, \dots, t_T^l)$ corresponds to the motion tokens at level l , with T being the number of time steps. The term $\mathbf{t}_{<}^l$ denotes the causal context of \mathbf{t}^l , i.e., all tokens preceding the current position. The model p_θ , parameterized by weights θ , is trained to predict each token autoregressively based on its past tokens and the shared condition c . This objective encourages consistent hierarchical structure and smooth temporal evolution across all levels.

D. Infinite-Length Generation

By leveraging MoSA-VQ’s temporally discrete codes and RQHC’s autoregressive decoding, our framework naturally supports infinite-length motion generation from arbitrary time steps. During extension, the model conditions on previously generated tokens (excluding the original prompt embedding), while allowing the text prompt to be substituted dynamically—enabling seamless continuation under updated instructions.

a) Flexible Continuation with Prompt Switching.: At any generation step n , given an existing motion token sequence $\mathbf{t}_l^{1:n-1} = (t_1^1, t_2^1, \dots, t_{n-1}^1)$ at quantization level l , we continue autoregressive generation from step n onward using the RQHC-Transformer. To support runtime intervention, we allow prompt switching by replacing the original text condition \mathbf{p}_{old} with a new prompt \mathbf{p}_{new} , yielding an updated conditioning vector $c = \mathbf{p}_{\text{new}} + \mathbf{q}_{\text{emb}}$.

While the previous tokens $\mathbf{t}_l^{1:n-1}$ are preserved, the updated prompt influences subsequent decoding. At each step n ,

RQHC predicts the next token t_i^n based on the causal context and the new condition:

$$t_i^n \sim p_\theta(t_i^n | \mathbf{t}_i^{1:n-1}, c), \quad \forall n > n-1. \quad (9)$$

This per-step decoding continues autoregressively and can be extended to arbitrary lengths, enabling real-time motion continuation from any point. Crucially, the updated prompt takes effect immediately from step n , without requiring regeneration of prior tokens. Only after completing the desired generation (of any length) do we perform motion decoding to reconstruct full-body trajectories. This design enables flexible, prompt-controllable extension with temporal coherence and efficient computation.

b) Why This Works.: This flexible and prompt-adaptive generation capability stems from the close architectural synergy between MoSA-VQ and RQHC-Transformer. MoSA-VQ’s residual quantization provides a structured representation where coarse global motion is captured in early levels and finer dynamics are encoded hierarchically. This layered encoding ensures stability during long-horizon generation, as new content naturally extends existing motion without disrupting overall structure. In advanced, RQHC’s hierarchical causal structure enables prompt substitution at any point by conditioning future generation on preserved prior tokens, ensuring smooth semantic transitions. Together, these properties support real-time extension, runtime editing, and infinite-length motion generation under evolving conditions.

E. Text Condition Alignment for Improved Motion Decoding

Real-world user prompts for motion generation often deviate from the structured annotations seen during training, varying in style, verbosity, and semantic complexity. Notably, many instructions contain abstract or composite motions that are difficult to execute when treated as a single condition, posing a fundamental challenge to robust generation.

To bridge this gap, we propose TCA, an inference-time strategy that leverages a pretrained large language model \mathcal{T} to enhance both interpretability and executability of free-form prompts—without modifying model parameters. TCA performs two key functions: (1) *style normalization*, aligning user input with the model’s linguistic prior, and (2) *instruction decomposition*, splitting complex intents into atomic motion steps.

Formally, given an arbitrary user prompt $\mathbf{c}_{\text{raw}} \in \mathbb{U}$, TCA first produces a normalized instruction $\mathbf{c}_{\text{norm}} \in \mathbb{S}$, then applies Chain-of-Thought prompting over \mathcal{T} to decompose it as:

$$[\mathbf{c}^{(1)}, \mathbf{c}^{(2)}, \dots, \mathbf{c}^{(K)}] = \mathcal{T}(\mathbf{c}_{\text{norm}} | \Psi_{\text{CoT}}), \quad (10)$$

where Ψ_{CoT} encodes few-shot exemplars and reasoning patterns.

Each $\mathbf{c}^{(k)}$ denotes a semantically atomic sub-instruction, enabling the motion model to synthesize sequences in a stepwise or joint manner with improved controllability, precision, and temporal coherence.

By externally structuring complex instructions into executable units, TCA enhances generation quality across both seen and unseen prompts—without requiring any fine-tuning or additional supervision.

IV. EXPERIMENTS

We comprehensively evaluate our MOGO framework on text-to-motion generation tasks, focusing on motion quality, text-motion alignment, and generalization. Additional experimental results and ablation studies are provided in the appendix for further analysis.

A. Datasets and Evaluation Metrics

1) Datasets: We train and evaluate MOGO on two widely used benchmarks, HumanML3D [17] and KIT-ML [31], following the data splits of T2M [17]. To assess out-of-distribution generalization, we further evaluate zero-shot performance on CMP [32], which contains non-daily, combat-style motions. Prompt engineering is disabled during CMP evaluation to ensure fairness.

2) Evaluation Metrics: We adopt standard metrics from [17]. *FID* (Frechet Inception Distance) measures motion realism and serves as a primary evaluation metric. *R-Precision* evaluates text-motion alignment (Top-1, 2, 3). *MM-Dist* computes the distance between motion and text embeddings. *MultiModality* measures the variance of motions generated from the same text prompt.

3) Training Details: The codebook is sized at 8192×128 with 6 quantization layers, using stride-1 convolutions and 0.2 dropout. It is trained with AdamW (learning rate 2×10^{-4} , batch size 512) for 2000 iterations on an NVIDIA 4090 GPU. RQHC-Transformer has 6 sub-modules aligned with RVQ layers, with head counts [16, 12, 6, 2, 2, 2] and layer counts [18, 16, 8, 4, 2, 2], and a model dimension of 1024. For HumanML3D, it is trained on an A800-80G with cosine decay from 2.5×10^{-5} to 3×10^{-6} , batch size 32, for 1500 epochs. For KIT-ML, a V100-32G is used with a learning rate from 3×10^{-5} to 3×10^{-6} , batch size 48.

B. Comparison to State-of-the-art Approaches

As shown in Figure 2, motions produced by our model are more semantically consistent with the input descriptions and exhibit smoother, more stable transitions without noticeable spatial drift. Additional qualitative visualizations, including extended motion generation results, are provided in the Appendix.

1) Reconstruction Quality of Motion Encoder: We compare our VAE design with existing motion VAEs—M2DM, T2M-GPT, MoMask, and MMM—on HumanML3D and KIT-ML (Table II). MOGO achieves the best results on both benchmarks, with an FID of 0.013 on HumanML3D, outperforming MoMask (0.019) and others. On the more challenging KIT-ML dataset, MOGO achieves an FID of 0.037, significantly lower than MoMask (0.112), T2M-GPT (0.472), and MMM (0.641). These results demonstrate the strong reconstruction capability of our VAE across diverse motion distributions.

2) Quantitative Results.: MOGO demonstrates strong performance across HumanML3D, KIT-ML, and zero-shot CMP benchmarks, particularly on FID and R@3. As shown in Table I, On HumanML3D, our base model achieves an FID of 0.038, outperforming T2M-GPT (0.116), MotionGPT (0.232),

TABLE I: Comparison with Motion Generation Models. **Boxed** = Best, **Bold** = Second Best, Underline = Third Best.

Datasets	Methods	R Precision \uparrow			FID \downarrow	MultiModal Dist \downarrow	MultiModality \uparrow
		Top 1	Top 2	Top 3			
HumanML3D	MotionDiffuse [19]	0.491 \pm 0.001	0.681 \pm 0.001	0.782 \pm 0.001	0.630 \pm 0.001	3.113 \pm 0.001	1.553 \pm 0.042
	T2M-GPT \dagger [3]	0.491 \pm 0.003	0.680 \pm 0.002	0.775 \pm 0.002	0.116 \pm 0.004	3.118 \pm 0.011	1.856 \pm 0.011
	Fg-T2M [29]	0.492 \pm 0.002	0.683 \pm 0.003	0.783 \pm 0.003	0.243 \pm 0.019	3.109 \pm 0.007	1.614 \pm 0.049
	AttT2M \dagger [5]	0.499 \pm 0.005	0.690 \pm 0.006	0.786 \pm 0.004	0.112 \pm 0.004	3.038 \pm 0.016	<u>2.452</u> \pm 0.043
	MotionGPT \dagger [22]	0.492 \pm 0.003	0.681 \pm 0.003	0.778 \pm 0.002	0.232 \pm 0.008	3.096 \pm 0.009	2.008 \pm 0.084
	MoMask [2]	0.521 \pm 0.002	0.713 \pm 0.002	0.807 \pm 0.002	0.045 \pm 0.002	2.958 \pm 0.008	1.241 \pm 0.040
	MMM [4]	0.504 \pm 0.002	0.696 \pm 0.003	0.794 \pm 0.004	0.080 \pm 0.004	2.998 \pm 0.007	1.226 \pm 0.035
	MotionAnything [30]	0.546 \pm 0.002	0.735 \pm 0.002	0.829 \pm 0.002	0.028 \pm 0.001	2.859 \pm 0.010	2.705 \pm 0.060
	MOGO \dagger	0.515 \pm 0.003	0.709 \pm 0.003	0.801 \pm 0.003	0.064 \pm 0.002	2.951 \pm 0.008	2.108 \pm 0.070
	MOGO with TCA \dagger	<u>0.527</u> \pm 0.007	<u>0.722</u> \pm 0.008	<u>0.827</u> \pm 0.012	<u>0.038</u> \pm 0.003	2.849 \pm 0.003	2.344 \pm 0.037
KIT-ML	MotionDiffuse [19]	0.417 \pm 0.004	0.621 \pm 0.004	0.739 \pm 0.004	1.954 \pm 0.062	2.958 \pm 0.005	0.730 \pm 0.013
	T2M-GPT \dagger [3]	0.416 \pm 0.006	0.627 \pm 0.006	0.745 \pm 0.006	0.514 \pm 0.029	3.007 \pm 0.023	1.570 \pm 0.039
	Fg-T2M [29]	0.418 \pm 0.005	0.626 \pm 0.004	0.745 \pm 0.004	0.571 \pm 0.047	3.114 \pm 0.015	1.019 \pm 0.029
	AttT2M \dagger [5]	0.413 \pm 0.006	0.632 \pm 0.006	0.751 \pm 0.006	0.870 \pm 0.039	3.039 \pm 0.016	<u>2.281</u> \pm 0.043
	MotionGPT \dagger [22]	0.366 \pm 0.005	0.558 \pm 0.004	0.680 \pm 0.005	0.510 \pm 0.004	3.527 \pm 0.021	2.328 \pm 0.117
	MoMask [2]	0.433 \pm 0.007	0.656 \pm 0.005	0.781 \pm 0.005	0.204 \pm 0.011	2.779 \pm 0.022	1.131 \pm 0.043
	MMM [4]	0.381 \pm 0.005	0.590 \pm 0.006	0.718 \pm 0.005	0.429 \pm 0.019	3.146 \pm 0.019	1.105 \pm 0.026
	MotionAnything [30]	0.449 \pm 0.007	0.678 \pm 0.004	0.802 \pm 0.006	0.131 \pm 0.003	2.705 \pm 0.024	1.374 \pm 0.060
	MOGO \dagger	0.420 \pm 0.007	0.634 \pm 0.007	0.754 \pm 0.007	0.313 \pm 0.016	2.957 \pm 0.029	2.063 \pm 0.066
	MOGO with TCA \dagger	<u>0.447</u> \pm 0.023	<u>0.668</u> \pm 0.016	<u>0.801</u> \pm 0.007	<u>0.191</u> \pm 0.009	2.849 \pm 0.007	2.273 \pm 0.073
CMP (zero-shot)	T2M-GPT \dagger [3]	0.061 \pm 0.003	0.103 \pm 0.005	0.147 \pm 0.006	16.092 \pm 0.099	4.179 \pm 0.049	2.118 \pm 0.033
	AttT2M \dagger [5]	0.065 \pm 0.004	0.109 \pm 0.008	0.147 \pm 0.008	18.403 \pm 0.071	4.048 \pm 0.017	2.208 \pm 0.019
	MotionGPT \dagger [22]	0.050 \pm 0.002	0.094 \pm 0.002	0.133 \pm 0.003	<u>15.654</u> \pm 0.183	4.431 \pm 0.021	5.535 \pm 0.259
	MoMask [2]	0.062 \pm 0.003	0.108 \pm 0.005	0.150 \pm 0.004	24.351 \pm 0.205	4.817 \pm 0.022	1.651 \pm 0.050
	MMM [4]	<u>0.067</u> \pm 0.004	<u>0.116</u> \pm 0.008	<u>0.154</u> \pm 0.008	17.087 \pm 0.313	4.360 \pm 0.017	2.802 \pm 0.011
	MOGO \dagger	0.071 \pm 0.003	0.124 \pm 0.004	0.183 \pm 0.004	10.388 \pm 0.171	3.847 \pm 0.029	4.562 \pm 0.066
	MOGO with TCA \dagger	0.122 \pm 0.006	0.227 \pm 0.011	0.304 \pm 0.004	6.873 \pm 0.073	3.040 \pm 0.014	4.299 \pm 0.013

TABLE II: Comparison of reconstruction quality between our VAE design and prior motion VAEs.

HumanML3D		KIT-ML	
Method	FID \downarrow	Method	FID \downarrow
M2DM	0.063 \pm 0.001	M2DM	0.413 \pm 0.009
T2M-GPT	0.070 \pm 0.001	T2M-GPT	0.472 \pm 0.011
MoMask	0.019 \pm 0.001	MoMask	0.112 \pm 0.002
MMM	0.075 \pm 0.001	MMM	0.641 \pm 0.014
MOGO (ours)	0.013 \pm 0.001	MOGO (ours)	0.037 \pm 0.001

and MotionDiffuse (0.630). With TCA, FID slightly increases to 0.064, while R@3 improves from 0.801 to 0.827. On KIT-ML, MOGO attains an FID of 0.191 and R@3 of 0.801, competitive with MotionAnything (FID 0.131, R@3 0.802). Under the zero-shot CMP setting, FID drops to 10.388 (6.873 with TCA), outperforming MotionGPT (15.654) and T2M-GPT (16.092), while R@3 reaches 0.304, over twice that of the best baseline MMM (0.154).

Overall, our method consistently achieves top FID and R@3 scores across benchmarks. The TCA module further enhances semantic alignment, especially under distribution shifts, validating the effectiveness of structured condition interpretation.

C. Ablation Study

1) *Ablation Study on VAE Depth:* We evaluate the impact of quantization depth by varying the number of layers while fixing the codebook size to 8192×128 (Table VIII). A single-layer quantizer performs poorly (FID: 0.070), indicating

TABLE III: The impact of different quantization layers on model reconstruction quality when the codebook size is 8192×128 . Bold face indicates the best result.

Depth	FID \downarrow	R TOPI \uparrow	MM-Dist \downarrow
1	0.070 \pm 0.001	0.502 \pm 0.001	2.999 \pm 0.006
3	0.021 \pm 0.001	0.508 \pm 0.001	2.992 \pm 0.008
6	0.016 \pm 0.001	0.510 \pm 0.001	2.989 \pm 0.007
7	0.016 \pm 0.001	0.509 \pm 0.001	2.996 \pm 0.003

limited capacity. Increasing to 3 layers significantly improves performance (FID: 0.021), and 6 layers yields the best overall results (FID: **0.016**, R@1: 0.510, MM-Dist: 2.989). Adding a 7th layer offers no further gain and slightly worsens MM-Dist, suggesting diminishing returns. Overall, 6-layer quantization provides the best balance between expressiveness and generalization.

2) *Ablation Study on Layer-Head Configuration:* We study the impact of Transformer depth and attention head configurations on HumanML3D (Table IV). Starting from a uniform setup ([4, 4, 4, 4, 4, 4] layers, [6, 6, 6, 6, 6, 6] heads), the model yields suboptimal results (FID 0.101, MM-Dist 3.359). As we adopt deeper, hierarchically structured layers and progressively narrower heads, performance improves consistently. The best configuration ([18, 16, 8, 4, 2, 2] layers, [16, 12, 6, 2, 2, 2] heads) achieves the lowest FID (**0.079**), highest R@1 (**0.505**), and lowest MM-Dist (**3.002**).

These findings suggest that allocating more depth in early

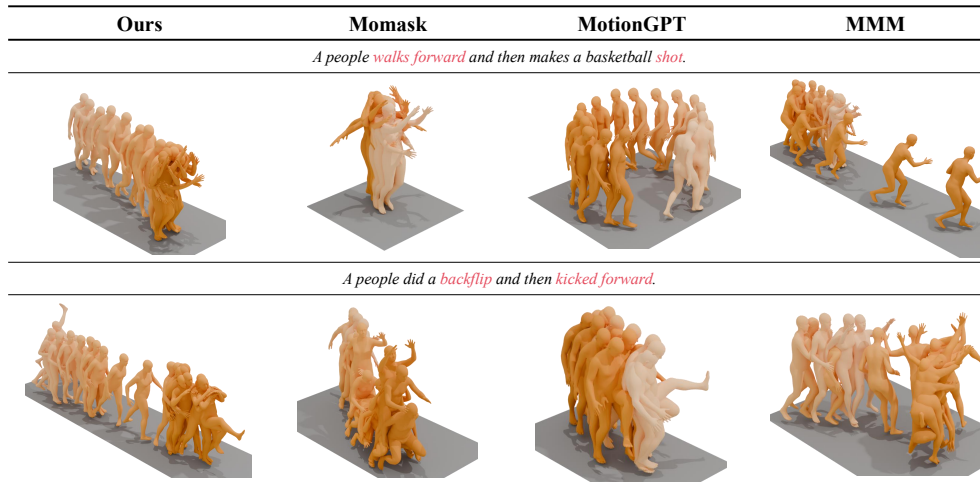


Fig. 2: Qualitative comparison of generated motions produced by different models. Compared to prior methods Momask, MotionGPT, and MMM.

TABLE IV: Impact of model depths and head configurations on HumanML3D results (codebook size: 8192×128). Bold indicates the best performance.

Heads	Layers	FID↓	R@1↑	MM-Dist↓
[4, 4, 4, 4, 4, 4]	[6]	0.242±0.009	0.397±0.005	4.132±0.013
[4, 4, 4, 4, 4, 4]	[6, 6, 6, 6, 6, 6]	0.101±0.004	0.461±0.003	3.359±0.009
[12, 6, 4, 2, 2, 2]	[16, 8, 6, 4, 2, 2]	0.077±0.003	0.473±0.003	3.260±0.010
[16, 8, 4, 2, 2, 2]	[18, 10, 6, 4, 2, 2]	0.058±0.003	0.490±0.002	3.168±0.009
[16, 12, 4, 2, 2, 2]	[18, 16, 6, 4, 2, 2]	0.044±0.004	0.508±0.003	3.063±0.010
[16, 12, 6, 2, 2, 2]	[18, 16, 8, 4, 2, 2]	0.038±0.002	0.515±0.003	2.951±0.008

stages and gradually reducing head width enables better modeling of both global semantics and local temporal details. Compared to uniformly scaled variants, hierarchical designs yield stronger R@1 and MM-Dist, highlighting the importance of architectural balance.

For more ablation details, please check our Appendix.

V. CONCLUSION

We presented MOGO, a one-pass autoregressive framework for high-quality and real-time 3D human motion generation. By combining the MoSA-VQ module for scale-adaptive residual vector quantization with the RQHC-Transformer for hierarchical causal decoding, MOGO achieves efficient and temporally coherent motion synthesis. The integration of TCA mechanism further enhances semantic alignment and enables better generalization in zero- and few-shot scenarios. Our framework supports low-latency, frame-by-frame inference, making it well-suited for real-time and interactive applications. Extensive experiments demonstrate that MOGO consistently outperforms prior transformer-based methods across multiple benchmarks in terms of generation quality and text-motion

alignment, establishing a strong foundation for future research on controllable, editable, and interactive motion generation.

REFERENCES

- [1] W. Zhu, X. Ma, D. Ro, H. Ci, J. Zhang, J. Shi, F. Gao, Q. Tian, and Y. Wang, “Human motion generation: A survey,” *IEEE Transactions on Pattern Analysis and Machine Intelligence*, vol. 46, no. 4, pp. 2430–2449, 2023. I, II
- [2] C. Guo, Y. Mu, M. G. Javed, S. Wang, and L. Cheng, “Momask: Generative masked modeling of 3d human motions,” in *Proceedings of the IEEE/CVF Conference on Computer Vision and Pattern Recognition*, 2024, pp. 1900–1910. I, II, III-B, I
- [3] J. Zhang, Y. Zhang, X. Cun, Y. Zhang, H. Zhao, H. Lu, X. Shen, and Y. Shan, “Generating human motion from textual descriptions with discrete representations,” in *Proceedings of the IEEE/CVF conference on computer vision and pattern recognition*, 2023, pp. 14730–14740. I, II, I
- [4] E. Pinyoanuntapong, P. Wang, M. Lee, and C. Chen, “Mmm: Generative masked motion model,” in *Proceedings of the IEEE/CVF Conference on Computer Vision and Pattern Recognition*, 2024, pp. 1546–1555. I, II, I
- [5] C. Zhong, L. Hu, Z. Zhang, and S. Xia, “Att2m: Text-driven human motion generation with multi-perspective attention mechanism,” in *Proceedings of the IEEE/CVF International Conference on Computer Vision*, 2023, pp. 509–519. I, II, III-B, I
- [6] G. Tevet, S. Raab, B. Gordon, Y. Shafir, D. Cohen-Or, and A. H. Bermano, “Human motion diffusion model,” *arXiv preprint arXiv:2209.14916*, 2022. I, II
- [7] R. Rombach, A. Blattmann, D. Lorenz, P. Esser, and B. Ommer, “High-resolution image synthesis with latent diffusion models,” in *Proceedings of the IEEE/CVF Conference on Computer Vision and Pattern Recognition (CVPR)*. New Orleans, LA, USA: IEEE, June 2022, pp. 10684–10695, arXiv:2112.10752. I
- [8] X. Chen, B. Jiang, W. Liu, Z. Huang, B. Fu, T. Chen, and G. Yu, “Executing your commands via motion diffusion in latent space,” in *Proceedings of the IEEE/CVF conference on computer vision and pattern recognition*, 2023, pp. 18000–18010. I, II
- [9] T. Brown, B. Mann, N. Ryder, M. Subbiah, J. D. Kaplan, P. Dhariwal, A. Neelakantan, P. Shyam, G. Sastry, A. Askell *et al.*, “Language models are few-shot learners,” *Advances in neural information processing systems*, vol. 33, pp. 1877–1901, 2020. I
- [10] C. Raffel, N. Shazeer, A. Roberts, K. Lee, S. Narang, M. Matena, Y. Zhou, W. Li, and P. J. Liu, “Exploring the limits of transfer learning with a unified text-to-text transformer,” *Journal of machine learning research*, vol. 21, no. 140, pp. 1–67, 2020. I
- [11] C. Ahuja and L.-P. Morency, “Language2pose: Natural language grounded pose forecasting,” in *2019 International conference on 3D vision (3DV)*. IEEE, 2019, pp. 719–728. II

- [12] A. Ghosh, N. Cheema, C. Oguz, C. Theobalt, and P. Slusallek, "Synthesis of compositional animations from textual descriptions," in *Proceedings of the IEEE/CVF international conference on computer vision*, 2021, pp. 1396–1406. II
- [13] H. Cai, C. Bai, Y.-W. Tai, and C.-K. Tang, "Deep video generation, prediction and completion of human action sequences," in *Proceedings of the European conference on computer vision (ECCV)*, 2018, pp. 366–382. II
- [14] Z. Wang, P. Yu, Y. Zhao, R. Zhang, Y. Zhou, J. Yuan, and C. Chen, "Learning diverse stochastic human-action generators by learning smooth latent transitions," in *Proceedings of the AAAI conference on artificial intelligence*, vol. 34, no. 07, 2020, pp. 12 281–12 288. II
- [15] C. Guo, X. Zuo, S. Wang, X. Liu, S. Zou, M. Gong, and L. Cheng, "Action2video: Generating videos of human 3d actions," *International Journal of Computer Vision*, vol. 130, no. 2, pp. 285–315, 2022. II
- [16] M. Petrovich, M. J. Black, and G. Varol, "Action-conditioned 3d human motion synthesis with transformer vae," in *Proceedings of the IEEE/CVF International Conference on Computer Vision*, 2021, pp. 10 985–10 995. II
- [17] C. Guo, S. Zou, X. Zuo, S. Wang, W. Ji, X. Li, and L. Cheng, "Generating diverse and natural 3d human motions from text," in *Proceedings of the IEEE/CVF conference on computer vision and pattern recognition*, 2022, pp. 5152–5161. II, IV-A1, IV-A2, VII
- [18] J. Kim, J. Kim, and S. Choi, "Flame: Free-form language-based motion synthesis & editing," in *Proceedings of the AAAI Conference on Artificial Intelligence*, vol. 37, no. 7, 2023, pp. 8255–8263. II
- [19] M. Zhang, Z. Cai, L. Pan, F. Hong, X. Guo, L. Yang, and Z. Liu, "Motiondiffuse: Text-driven human motion generation with diffusion model," *IEEE transactions on pattern analysis and machine intelligence*, vol. 46, no. 6, pp. 4115–4128, 2024. II, I
- [20] M. Zhang, X. Guo, L. Pan, Z. Cai, F. Hong, H. Li, L. Yang, and Z. Liu, "Remodiffuse: Retrieval-augmented motion diffusion model," in *Proceedings of the IEEE/CVF International Conference on Computer Vision*, 2023, pp. 364–373. II
- [21] H. Kong, K. Gong, D. Lian, M. B. Mi, and X. Wang, "Priority-centric human motion generation in discrete latent space," in *Proceedings of the IEEE/CVF International Conference on Computer Vision*, 2023, pp. 14 806–14 816. II
- [22] B. Jiang, X. Chen, W. Liu, J. Yu, G. Yu, and T. Chen, "Motiongpt: Human motion as a foreign language," *Advances in Neural Information Processing Systems*, vol. 36, pp. 20 067–20 079, 2023. II, I
- [23] P. Nawrot, S. Tworkowski, M. Tyrolski, Ł. Kaiser, Y. Wu, C. Szegedy, and H. Michalewski, "Hierarchical transformers are more efficient language models," in *Findings of the Association for Computational Linguistics: NAACL 2022*, 2022, pp. 1559–1571. II
- [24] R. Pappagari, P. Żelasko, J. Villalba, Y. Carmiel, and N. Dehak, "Hierarchical transformers for long document classification," in *2019 IEEE Automatic Speech Recognition and Understanding Workshop (ASRU)*. Singapore: IEEE, December 2019, pp. 838–844, arXiv:1910.10781. II
- [25] M. Ding, W. Zheng, W. Hong, and J. Tang, "Cogview2: Faster and better text-to-image generation via hierarchical transformers," *Advances in Neural Information Processing Systems*, vol. 35, pp. 16 890–16 902, 2022. II
- [26] Z. Liu, Y. Lin, Y. Cao, H. Hu, Y. Wei, Z. Zhang, S. Lin, and B. Guo, "Swin transformer: Hierarchical vision transformer using shifted windows," in *Proceedings of the IEEE/CVF international conference on computer vision*, 2021, pp. 10 012–10 022. II
- [27] R. J. Chen, C. Chen, Y. Li, T. Y. Chen, A. D. Trister, R. G. Krishnan, and F. Mahmood, "Scaling vision transformers to gigapixel images via hierarchical self-supervised learning," in *Proceedings of the IEEE/CVF conference on computer vision and pattern recognition*, 2022, pp. 16 144–16 155. II
- [28] C. Guo, X. Zuo, S. Wang, and L. Cheng, "Tm2t: Stochastic and tokenized modeling for the reciprocal generation of 3d human motions and texts," in *European Conference on Computer Vision*. Springer, 2022, pp. 580–597. II
- [29] Y. Wang, Z. Leng, F. W. Li, S.-C. Wu, and X. Liang, "Fg-t2m: Fine-grained text-driven human motion generation via diffusion model," in *Proceedings of the IEEE/CVF International Conference on Computer Vision*, 2023, pp. 22 035–22 044. I
- [30] Z. Zhang, Y. Wang, W. Mao, D. Li, R. Zhao, B. Wu, Z. Song, B. Zhuang, I. Reid, and R. Hartley, "Motion anything: Any to motion generation," *arXiv preprint arXiv:2503.06955*, 2025. I
- [31] M. Plappert, C. Mandery, and T. Asfour, "The kit motion-language dataset," *Big data*, vol. 4, no. 4, pp. 236–252, 2016. IV-A1
- [32] Y. Liao, Y. Fu, Z. Cheng, and J. Wang, "Animationgpt: An aige tool for generating game combat motion assets," <https://github.com/fyyakaxy/AnimationGPT>, 2024. IV-A1
- [33] J. Wei, X. Wang, D. Schuurmans, M. Bosma, b. ichter, F. Xia, E. Chi, Q. V. Le, and D. Zhou, "Chain-of-thought prompting elicits reasoning in large language models," in *Advances in Neural Information Processing Systems*, S. Koyejo, S. Mohamed, A. Agarwal, D. Belgrave, K. Cho, and A. Oh, Eds., vol. 35. Curran Associates, Inc., 2022, pp. 24 824–24 837. [Online]. Available: https://proceedings.neurips.cc/paper_files/paper/2022/file/9d5609613524ecf4f15af0f7b31abca4-Paper-Conference.pdf A0b
- [34] T. Kojima, S. S. Gu, M. Reid, Y. Matsuo, and Y. Iwasawa, "Large language models are zero-shot reasoners," *Advances in neural information processing systems*, vol. 35, pp. 22 199–22 213, 2022. A0b
- [35] X. Wang, J. Wei, D. Schuurmans, Q. Le, E. Chi, S. Narang, A. Chowdhery, and D. Zhou, "Self-consistency improves chain of thought reasoning in language models," *arXiv preprint arXiv:2203.11171*, 2022. A0c

APPENDIX

A. Qualitative Results of Infinite Motion Generation.

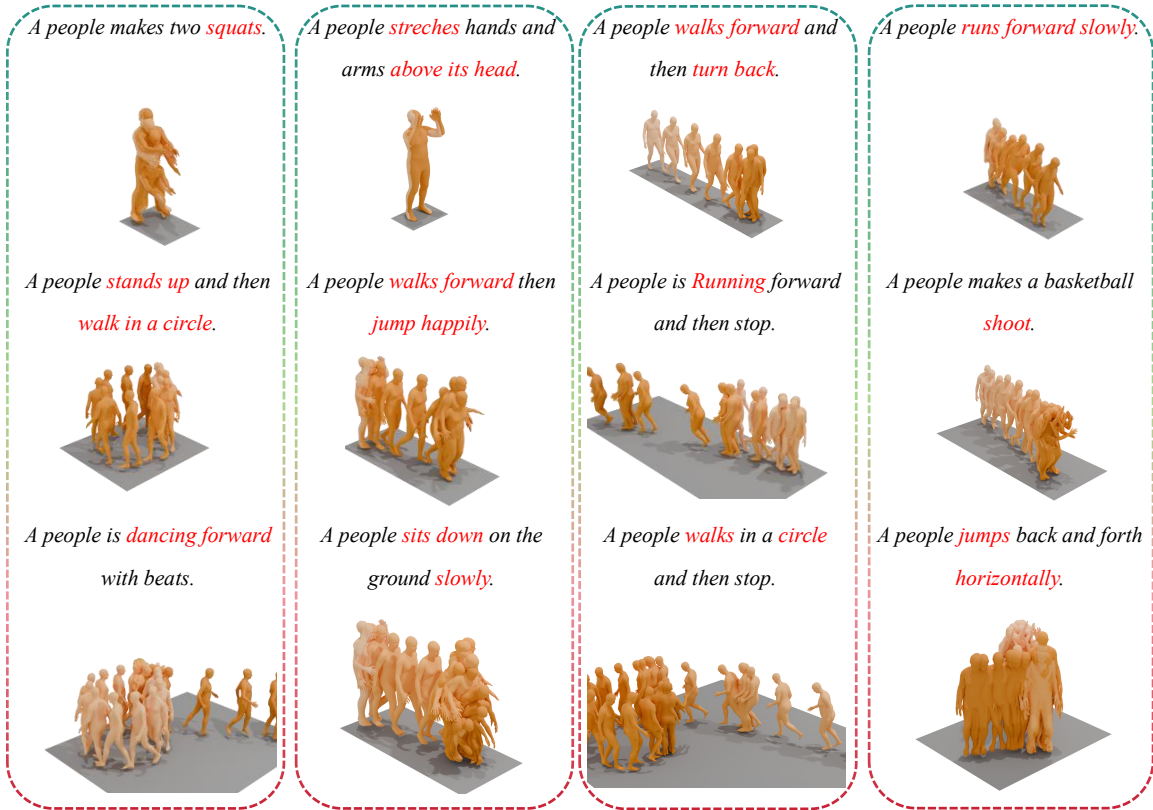


Fig. 3: Motion Extension during Inference.

Figure 3 showcases qualitative results of our infinite motion generation pipeline. Each vertical dashed box represents a complete generation sequence conditioned on a given text prompt. From top to bottom, the first row shows the initial motion segment, while the subsequent rows illustrate recursively generated motion continuations, conditioned on the same or semantically extended instruction.

Across all four examples, our model demonstrates strong temporal consistency, with smooth transitions between motion segments and no noticeable discontinuities. The generated motions exhibit high semantic fidelity to the input descriptions, such as complex behaviors like “walks in a circle and then stop”, “jumps back and forth horizontally”, or “dancing forward with beats”, all of which are well-executed over extended sequences. The smooth transition between action phrases (e.g., “stands up and then walk in a circle”) further indicates that our model captures both short-term dynamics and long-horizon dependencies effectively.

To support reproducibility and further inspection, we provide all visual examples shown in Figure 3 as rendered videos, along with additional qualitative results in the supplementary materials. Specifically, the included .zip file contains not only video renderings corresponding to the figure, but also additional extended generations for diverse prompts—several of which feature single uninterrupted motion sequences exceeding 2000 frames in length. These results further demonstrate the stability of our model in synthesizing temporally consistent and semantically aligned motion over prolonged durations.

These results highlight the model’s capability to generate coherent, instruction-aligned motion indefinitely, making it suitable for real-world applications like virtual agents, gaming, and embodied language understanding.

B. Qualitative Results of Single-Prompt Generation

Figure 4 presents a comprehensive overview of our model’s ability to generate motion sequences that align with a wide range of text prompts, demonstrating both semantic fidelity and fine-grained motion expressiveness. Each sample in the figure consists of a 3D motion mesh superimposed with motion trails (or motion blending) and its corresponding textual description, rendered in a stylized format where key action phrases are emphasized in red italics.



Fig. 4: Generation Results

a) *Semantic Diversity and Text-Condition Alignment.*: Across the 4×4 grid layout, we showcase 16 distinct prompts covering a diverse set of actions, such as:

- **Simple physical reactions:** “The person was pushed but did not fall.”
- **Complex multi-phase motions:** “A man is walking forward then steps over a stair then continues walking forward.”
- **Locomotion with intention shifts:** “walked forward spun right on one foot and walked back to his original position.”
- **Fine-grained bodily behaviors:** “holds their right foot with their right hand lifting both their left foot and left hand up.”
- **Stylized or culturally grounded motions:** “The person does a salsa dance.”
- **Emotionally expressive behaviors:** “A person walks with a limp, their right leg gets injured.”

These results indicate that our model is capable of capturing not only locomotion and spatial translation but also static poses, micro-movements, and non-trivial action transitions. The linguistic variations in the prompts are successfully translated into physically coherent movement, suggesting a high level of text-to-motion grounding.

b) *Motion Coherence and Realism.*: Visually, the rendered meshes show strong temporal consistency. The use of motion trails helps reveal the flow of the action over time, allowing readers to observe details such as:

- Symmetrical limb movement (as in treadmill running),
- Localized gestures (like jabbing with the hand),
- Balanced posture shifts (e.g., squatting while crossing the leg and lowering with both hands).

Each figure shows a stable, physically plausible movement trajectory. Particularly in examples like the limp walking or the foot-holding pose, the model demonstrates a robust understanding of joint constraints and biomechanical plausibility, which are often hard to synthesize accurately.

Moreover, the transitions between joint configurations remain smooth and contextually aligned. For instance, the action “walks forward then steps over a stair” is depicted not only as a forward movement but with a discernible vertical leg lift, capturing the semantic intent of stepping.

c) *Expressiveness and Subtle Behaviors.*: The model also demonstrates the ability to synthesize expressive and subtle behaviors from relatively short prompts. Examples such as:

- “blocks their face with their right arm”
- “stands, crosses their left leg in front...”

highlight the model’s capability to generate contextually appropriate and biomechanically accurate poses. These motions require localized articulation and fine control, which the model executes effectively.

C. Summary

In conclusion, Figure 4 provides compelling evidence of our model’s ability to generate temporally coherent, semantically grounded, and physically plausible motions across a wide range of instructions. The diversity of action types, from stylized dance to nuanced micro-movements, highlights its applicability to real-world embodied tasks such as virtual agents, assistive robots, and language-driven animation.



Fig. 5: Comparison of motion sequences generated with and without Text Condition Alignment (TCA). TCA improves temporal coherence and semantic clarity, yielding more realistic and faithful motions.

APPENDIX

A. Prompt-Engineering Strategy

TCA relies on a *single* LLM call whose prompt is carefully engineered to yield: (i) a normalized, imperative restatement of the user request, (ii) a line-separated sequence of atomic motion steps, and (iii) a final rewritten instruction that merges all atomic actions into a fluent, single-sentence command with an explicit subject (e.g., “A person lifts both arms, swings them forward in an arc, and returns to a standing position”). The design combines several complementary techniques:

a) *S1. Role & Goal Priming.*: We begin with an explicit role declaration: “*You are an instruction rewriter for a motion-generation robot.*” This is immediately followed by a goal statement: “*Transform the user request into a concise command (Normalized), a numbered list of executable steps (Steps), and a final rewritten instruction combining all actions into a single fluent sentence with a human subject.*” This dual priming has two effects: (1) it reduces style drift across diverse user inputs, and (2) it biases the LLM toward a structured, imperative language style aligned with the motion decoder’s text prior.

b) *S2. Chain-of-Thought (CoT) Cueing — Two-Stage Least-to-Most Prompting.*: To obtain reliable, atomic motion commands without revealing the LLM’s private reasoning, we implement a lightweight *Least-to-Most* (LtM) procedure. The complete CoT [33] prompt is executed within a **single** API call but is conceptually divided into two internal stages:

S2.1 Intent Decomposition. The model is first instructed: “*Think step by step. Rewrite the user request as one concise imperative sentence, then list the minimal executable actions, one per line, and finally output a single-sentence rewritten instruction beginning with ‘A person ...’ that combines all the actions. Do not reveal your reasoning.*” This stage encourages hidden chain-of-thought while enforcing a deterministic, three-part output schema [34].

S2.2 Self-Verification & Refinement. Immediately after producing the draft list, the prompt appends: “*Verify that every step can be executed in isolation by a humanoid motion agent. If any step is composite or ambiguous, split it further and rewrite the entire list and the final sentence accordingly.*” The model then overwrites its own answer before the final stop token, yielding a refined set of atomic steps and a natural-language instruction that summarizes them with an explicit subject.

c) *S3. Few-Shot Curriculum (In-Context Learning).*: To equip the LLM with a prior on how free-form descriptions in our dataset should be reformulated into structured commands, we perform a lightweight *in-context learning* (ICL) setup. Specifically, we prepend three demonstration pairs to every query, sampled directly from our training corpus and rewritten into the target schema (Normalized + Steps + Final instruction). These demonstrations jointly span diverse [35] *syntax*—casual narration, imperative clause, and run-on sentence—and heterogeneous *semantics*—dance, locomotion, and object interaction. The curriculum is designed to:

- expose the model to prompts consistent with the training data distribution, encouraging flexible segmentation into 2–5 atomic steps;
- illustrate how varied tense and verbosity in raw captions can be normalized into concise imperative commands and rewritten human-centric instructions;
- include both prompts with and without implicit pauses, teaching the model to insert explicit *hold* actions when necessary.

Action verbs in the demonstrations are drawn from the motion model’s training vocabulary, ensuring lexical consistency between the rewritten instructions and the downstream decoder, while requiring *no* parameter modifications. This ICL design narrows the style gap between descriptive captions in the dataset and real user prompts, improving controllability during TCA inference.

B. Qualitative Examples

a) *Example 1. (Humanml3D Test):*

- **Raw prompt:** “*Someone imitating a golf swing.*”
- **Normalized:** “*Raise arms, swing forward, return to stance.*”
- **Thinking process:**
 1. Lift both arms as if holding a golf club
 2. Swing the arms forward in an arc
 3. Return to a relaxed standing posture
- **Final rewritten instruction:** “*A person lifts both arms, swings them forward in an arc, and returns to a standing position.*”

b) *Example 2. (Wild data Test):*

- **Raw prompt:** “*A human is practicing expressive spinning gestures.*”
- **Normalized:** “*Spin, pause, raise arms.*”
- **Steps:**
 1. Spin once on the spot
 2. Hold still for a beat

3. Raise both hands

- **Final rewritten instruction:**

“A person spins once on the spot, holds still briefly, and raises both hands.”

c) Example 3. (Wild data Test):

- **Raw prompt:** *“A human is rehearsing a dynamic forward motion sequence.”*

- **Normalized:** *“Walk, crouch, roll forward, stand.”*

- **Steps:**

1. Walk forward
2. Drop into a crouch
3. Roll forward
4. Stand upright

- **Final rewritten instruction:**

“A person walks forward, drops into a crouch, rolls ahead, and stands upright.”

As shown in Figure 5, these cases show how TCA strategy reliably converts noisy, multi-clause requests into concise, executable motion scripts—enabling the decoder to render complex behaviours with accurate temporal structure *without any motion-model fine-tuning*.

C. Impact of Learnable Scaling in MoSA-VQ.

We investigate the role of the proposed learnable scaling mechanism in MoSA-VQ by comparing models with and without this design. In the baseline configuration, residual features at each quantization level are directly quantized without any adaptive normalization. In contrast, our full model applies a layer-specific affine transformation before quantization, allowing each level to adjust the residual space dynamically. As shown in Table V, incorporating learnable scale and bias parameters leads to consistent improvements across multiple evaluation metrics. The model demonstrates better reconstruction quality, enhanced alignment between motion and text, and stronger semantic consistency. These results highlight the benefit of introducing adaptive normalization in residual quantization, which facilitates more expressive and stable token representations.

TABLE V: Ablation study on the use of learnable scaling. We evaluate various codebook sizes on HumanML3D.

w/ Learnable Scaling				w/o Learnable Scaling			
Codebook	FID↓	Top1↑	MM-Dist↓	Codebook	FID↓	Top1↑	MM-Dist↓
2048×512	0.052±0.005	0.498±0.002	2.997±0.008	2048×512	0.094±0.011	0.484±0.002	3.273±0.009
4096×256	0.047±0.005	0.501±0.002	2.901±0.008	4096×256	0.091±0.004	0.493±0.004	3.451±0.017
8192×128	0.038±0.003	0.515±0.007	2.951±0.003	8192×128	0.079±0.002	0.502±0.002	3.002±0.008

D. Impact of prompt and quantization.

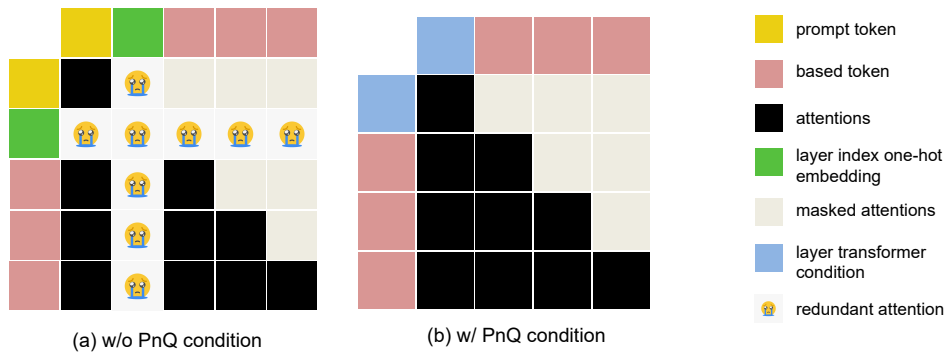


Fig. 6: Comparison of attention patterns with and without the PnQ (Prompt and Quantization) condition

1) *Without PnQ*: An additional layer token is inserted between the textual prompt and the quantized motion sequence, serving as an intermediate fusion node. However, this design introduces a level of indirection that leads to redundant attention computation and diluted gradient flow. As a result, the model exhibits weaker cross-modal alignment, as the semantic linkage between text and motion must be learned indirectly through this intermediate token, which may act as a bottleneck in representation transfer.

2) *With PnQ*: We instead fuse the prompt token directly with the quantization condition tokens through positional and conditional injection. This eliminates the need for an intermediate token and allows the model to establish a more direct and semantically grounded connection between the text prompt and motion representation. Consequently, this design not only improves attention efficiency—by reducing unnecessary detours in the attention graph—but also enhances the cross-modal alignment by preserving semantic consistency throughout the sequence.

E. Effect of Dataset Size

To investigate the scalability of MOGO, we evaluate its performance under different training set sizes by progressively mixing HumanML3D with 50% and 100% proportions of the CMP dataset. Crucially, we keep the MoSA-VQ quantizer frozen during this process to isolate the impact of data volume on the downstream generation quality.

As shown in Table VI(a), increasing the amount of training data leads to consistent improvements in FID across training epochs. For instance, at 100 training epochs, FID drops from 0.347 (with only HumanML3D) to 0.263 with 50% CMP, and further to 0.205 with full CMP integration. This trend holds across earlier epochs as well, demonstrating that larger and more diverse motion data helps the model generalize better, even without modifying the discrete representation space.

These results highlight the scalability and data efficiency of MOGO’s architecture, as well as the robustness of the MoSA-VQ quantizer in accommodating novel distributions through fixed codes.

TABLE VI: Left: Effect of dataset size on FID. Right: Real-time inference comparison on A800.

(a) Dataset Size vs. FID				(b) Real-time Inference (A800)			
Epochs	0% CMP	50% CMP	100% CMP	Method	AITs \uparrow	Params	FID \downarrow
50	0.671	0.601	0.501	MLD	0.14	34M	0.473
80	0.437	0.379	0.284	MotionGPT	0.81	770M	0.160
100	0.347	0.263	0.205	MoMask	0.06	163M	0.045
				MOGO	0.37	830M	0.038

F. Real-Time Inference Efficiency

We evaluate the inference efficiency of MOGO by measuring the average time required to generate a full motion sequence of 196 frames per input sentence, denoted as Average Inference Time per Sentence (AITs). As shown in Table VI(b), we compare our model with several state-of-the-art methods under consistent hardware (single A800 GPU).

MOGO achieves an average inference time of 0.37 seconds per sentence, demonstrating its ability to generate long-form motion in near real-time. While MoMask is faster due to its significantly smaller architecture, it delivers inferior performance in motion quality compared to MOGO. Conversely, methods like MotionGPT and MLD either trade off fidelity or speed, with MLD exceeding typical latency thresholds for interactive applications.

Despite its large parameter size (830M), MOGO produces the highest motion quality (FID = 0.038) among all methods while maintaining a latency level that is well-suited for real-time deployment in applications such as virtual avatars, embodied agents, and interactive character control.

These results confirm that MOGO is not only state-of-the-art in generation quality, but also practically deployable in real-time or near-real-time environments.

G. Effect of Codebook Size

TABLE VII: Study on the number of codes in codebook on HumanML3D [17] test set. **Bold** indicates the best FID result.

Codebook Size	Reconstruction			Generation		
	FID \downarrow	Top1 \uparrow	MM-Dist \downarrow	FID \downarrow	Top1 \uparrow	MM-Dist \downarrow
512 \times 512	0.022 \pm 0.001	0.508 \pm 0.003	2.997 \pm 0.007	0.203 \pm 0.009	0.469 \pm 0.002	3.138 \pm 0.006
1024 \times 1024	0.015 \pm 0.001	0.511 \pm 0.002	2.984 \pm 0.010	0.114 \pm 0.008	0.467 \pm 0.003	3.114 \pm 0.009
2048 \times 512	0.017 \pm 0.001	0.511 \pm 0.003	2.980 \pm 0.007	0.052 \pm 0.005	0.498 \pm 0.002	2.997 \pm 0.008
4096 \times 256	0.019 \pm 0.001	0.510 \pm 0.002	2.989 \pm 0.006	0.047 \pm 0.005	0.501 \pm 0.002	2.901 \pm 0.008
8192 \times 128	0.013 \pm 0.001	0.510 \pm 0.002	2.989 \pm 0.007	0.038 \pm 0.003	0.515 \pm 0.007	2.951 \pm 0.003

We conduct an ablation study to investigate how different codebook sizes affect both reconstruction and generation quality. Specifically, we vary the number of entries and dimensions in the codebook, and evaluate performance on the HumanML3D test set in terms of FID, Top-1 Accuracy, and MM-Distance. Results are summarized in Table VII.

As shown in the table, larger codebooks generally lead to better performance, particularly in the generation setting. When increasing the codebook size from 512 \times 512 to 8192 \times 128, the generation FID steadily decreases from 0.203 to 0.038, indicating a substantial improvement in motion realism. Similarly, Top-1 Accuracy improves from 0.469 to 0.515, and MM-Distance also decreases, suggesting enhanced semantic alignment and diversity.

In the reconstruction setting, we observe a similar trend: the FID drops from 0.022 to 0.013 as the codebook size increases. Notably, while some intermediate configurations (e.g., 1024 \times 1024) achieve marginally better reconstruction FID (0.015), they underperform in generation quality, highlighting that optimal reconstruction does not always translate to optimal generation.

The best overall performance is achieved with a codebook size of 8192 \times 128, which provides a favorable balance between code granularity and diversity. This configuration yields the lowest FID in both reconstruction and generation settings, while maintaining competitive Top-1 Accuracy and MM-Distance. These results demonstrate that increasing the expressiveness of the codebook—by enlarging its capacity—enables the quantizer to better capture fine-grained motion semantics and contributes to improved generative performance downstream.

H. Effect of Cross-Level Decorrelation Loss

To validate the effectiveness of our proposed cross-level decorrelation loss, we conduct an ablation experiment on the HumanML3D test set, as shown in Table VIII. We compare two settings: one using the full training objective (including \mathcal{L}_{decor}), and one without it.

TABLE VIII: We evaluate our decorrelation loss on HumanML3D

decorrelation loss	FID↓	R TOP1 ↑	MM-Dist↓
w/o	0.044±0.001	0.503 ±0.001	2.996 ±0.006
w/	0.038±0.001	0.508 ±0.001	2.992 ±0.008

When the decorrelation loss is removed, we observe a slight degradation in generation quality, with FID increasing from 0.038 to 0.044. Moreover, R-Top1 accuracy drops from 0.508 to 0.503, and MM-Distance increases from 2.992 to 2.996, indicating reduced semantic alignment and less precise generation.

This performance gap, although modest in absolute value, is consistent across all metrics and can be attributed to the inter-level redundancy present when $\mathcal{L}_{\text{decor}}$ is absent. As defined in Eq. (3), our decorrelation loss minimizes the batch-wise covariance between the quantized vector ϕ^l and the residual \mathbf{r}^{l+1} at the next level. This enforces statistical orthogonality across quantization layers, effectively disentangling the hierarchical representations.

From an information-theoretic standpoint, this encourages each level to capture novel, non-overlapping features, which reduces redundancy and improves latent code efficiency. In practice, this regularization leads to more compact and expressive codes—especially important under constrained codebook budgets or when deeper quantization hierarchies are used.

In summary, the proposed cross-level decorrelation loss plays a crucial role in enhancing both the semantic clarity and compression efficiency of our quantization framework, and leads to measurable improvements in motion generation quality.